Astronomy & Astrophysics manuscript no. output
January 8, 2020

TESS asteroseismology of the known planet host star λ^2 Fornacis

M.B. Nielsen[1,2,3], W.H. Ball[1,2], M.R. Standing[1], A.H.M.J. Triaud[1], D. Buzasi[4], L. Carboneau[4], K.G. Stassun[5], S.R. Kane[6], W.J. Chaplin[1,2], E.P. Bellinger[2,7], B. Mosser[8], I.W. Roxburgh[4,1], Z. Çelik Orhan[9], M. Yıldız[9], S. Örtel[9], M. Vrard[11,19], A. Mazumdar[20], P. Ranadive[20], M. Deal[11], G.R. Davies[1,2], T.L. Campante[11,12], R.A. García[13,14], S. Mathur[15,16], L. González Cuesta[15,16], and A. Serenelli[17,18]

[1] School of Physics and Astronomy, University of Birmingham, Birmingham B15 2TT, UK
e-mail: m.b.nielsen.1@bham.ac.uk
[2] Stellar Astrophysics Centre (SAC), Department of Physics and Astronomy, Aarhus University, Ny Munkegade 120, DK-8000 Aarhus C, Denmark
[3] Center for Space Science, NYUAD Institute, New York University Abu Dhabi, PO Box 129188, Abu Dhabi, United Arab Emirates
[4] Department of Chemistry and Physics, Florida Gulf Coast University, 10501 FGCU Blvd., Fort Myers, FL 33965 USA
[5] Department of Physics & Astronomy, Vanderbilt University, Nashville, TN 37235, USA
[6] Department of Earth and Planetary Sciences, University of California, Riverside, CA 92521, USA
[7] School of Physics, University of New South Wales, Kensington NSW 2033, Australia
[8] LESIA, Observatoire de Paris, Université PSL, CNRS, Sorbonne Université, Université de Paris, 92195 Meudon, France
[9] Department of Astronomy and Space Sciences, Science Faculty, Ege University, 35100, Bornova, İzmir, Turkey.
[10] Astronomy Unit, School of Physics and Astronomy, Queen Mary University of London, London E1 4NS, UK
[11] Instituto de Astrofísica e Ciências do Espaço, Universidade do Porto, Rua das Estrelas, 4150-762 Porto, Portugal
[12] Departamento de Física e Astronomia, Faculdade de Ciências da Universidade do Porto, Rua do Campo Alegre, s/n, 4169-007 Porto, Portugal
[13] IRFU, CEA, Université Paris-Saclay, F-91191 Gif-sur-Yvette, France
[14] AIM, CEA, CNRS, Université Paris-Saclay, Université Paris Diderot, Sorbonne Paris Cité, F-91191 Gif-sur-Yvette, France
[15] Instituto de Astrofísica de Canarias, La Laguna, Tenerife, Spain
[16] Dpto. de Astrofísica, Universidad de La Laguna, La Laguna, Tenerife, Spain
[17] Institute of Space Sciences (ICE, CSIC), Carrer de Can Magrans S/N, E-08193, Bellaterra, Spain
[18] Institut d'Estudis Espacials de Catalunya (IEEC), Carrer Gran Capita 2, E-08034, Barcelona, Spain
[19] Department of Astronomy, The Ohio State University, Columbus, OH 43210, USA
[20] Homi Bhabha Centre for Science Education, TIFR, V. N. Purav Marg, Mankhurd, Mumbai 400088, India

Received September 15, 1996; accepted March 16, 1997

ABSTRACT

Context. The Transiting Exoplanet Survey Satellite (TESS) is observing bright, known planet-host stars across almost the entire sky. These stars have been subject to extensive ground-based observations, providing a large number of radial velocity measurements.
Aims. The objective of this work is to use the new TESS photometric observations to characterize the star λ^2 Fornacis, and following this to update the parameters of the orbiting planet λ^2 For b.
Methods. We measure the frequencies of the *p*-mode oscillations in λ^2 For, and in combination with non-seismic parameters estimate the stellar fundamental properties using stellar models. Using the revised stellar properties and a time series of radial velocities collected from multiple instruments spanning almost 20 years, we refit the orbit of λ^2 For b and search the residual radial velocities for remaining variability.
Results. We find that λ^2 For has a mass of 1.16 ± 0.04 $M_\odot$ and a radius of 1.63 ± 0.04 $R_\odot$, making this a young sub-giant star with an age of 6.2 ± 0.9 Gyr. This and the updated radial velocity measurements suggest a mass of λ^2 For b of $16.8^{+1.2}_{-1.3}$ $M_\oplus$, which is $\sim 5M_\oplus$ less than literature estimates. We also detect an additional periodicity at 33 days in the radial velocity measurements, which is likely due to the rotation of the host star.
Conclusions. Even with a limited set of photometric data from TESS, we show that by using asteroseismology it is still possible to provide tight constraints on the properties of bright stars that have so far only been observed from the ground. This prompts a reexamination of archival radial velocity data that have been accumulated in the past few decades in order to update the characteristics of the planets orbiting these stars.

Key words. TESS– λ^2 Fornacis – asteroseismology – tbd

1. Introduction

The Transiting Exoplanet Survey Satellite (TESS, Ricker et al. 2014) has observed the southern celestial hemisphere in the period July 2018 to July 2019. The main objective of TESS is to observe short-period transiting exoplanets around bright stars. The observation strategy during the first year of operations has almost covered the entirety of the southern hemisphere, observing large swaths of the sky for short periods of time ($\approx$ 27 days). This is a departure from that of the previous space-based photometry missions CoRoT (Fridlund et al. 2006) and *Kepler* (Borucki et al. 2010), which provided photometric time series of hundreds of days or even several years for a few select fields. Such time

series have been a huge advantage for asteroseismology, which benefits from long observations and bright stars to make precise measurements of the oscillation modes of a star. The cohort of TESS targets extends to much brighter targets than *Kepler* and CoRoT, and so despite a lack of long baseline time series, the mission has already yielded a multitude of previously unknown variable stars, including solar-like oscillators.

The star, λ^2 Fornacis (HD 16417, λ^2 For), was initially selected for observation in the TESS two-minute cadence mode based on its brightness (G-band magnitude of 5.59) and high likelihood of exhibiting solar-like oscillations, as indicated by the Asteroseismic Target List (Schofield et al. 2019). It was observed for approximately 2 months shortly after the beginning of the TESS mission, and is one of the first planet-host stars to be observed by TESS with confirmed solar-like oscillations (see also Huber et al. 2019; Campante et al. 2019). Previous studies of λ^2 For have yielded a wide range of physical parameters (e.g., Bond et al. 2006; Gehren 1981; Bensby et al. 2014), indicating a spectral type anywhere between G2V or G8IV. Despite the relatively short amount of time that this star was observed by TESS, the photometric variability shows an unambiguous power excess at a frequency of $\approx 1280\,\mu$Hz, caused by solar-like acoustic (p-mode) oscillations. Stars with outer convective zones like the Sun and λ^2 For oscillate with regularly spaced overtones of radial and non-radial modes with angular degree, l. These modes propagate through the interior of the star and therefore place tight constraints on its physical properties (e.g. García & Ballot 2019). That the oscillation power of λ^2 For peaks at around $1280\,\mu$Hz alone places the star firmly in the sub-giant regime. However, going a step further and measuring the individual mode frequencies has been shown to yield estimates of the mass and radius at a precision of a few percent, and the stellar age at $\approx$ 10% (e.g., Brown et al. 1994; Lebreton & Goupil 2014; Angelou et al. 2017; Bellinger et al. 2019). This has implications for estimates of the characteristics of any potential orbiting planets, in particular with respect to the mass of the planets, but also in terms of the dynamical history of the system itself.

λ^2 For hosts a roughly Neptune-mass planet in a 17.25 day non-transiting orbit. The planet was discovered by O'Toole et al. (2009) using radial velocity (RV) measurements from the Anglo-Australian Telescope (AAT) and the Keck telescope. Since then an extensive set of HARPS (Mayor et al. 2003) data from the ESO La Silla 3.6m telescope has become publicly available. Here we combine the original observations by O'Toole et al. (2009) and the HARPS measurements to construct an almost 20 year set of RV data. This, combined with the updated estimates of the stellar mass from asteroseismology, allows us to better constrain the planet and its orbital parameters. Furthermore, the extensive RV data set also presents an opportunity to investigate variability at timescales other than the known planet.

The TESS time series reduction is presented in Section 2. The modeling process of λ^2 For is described in Section 3, including the power spectrum and SED fitting processes, which yields the seismic and non-seismic constraints respectively. In Section 4 we discuss the methods used to improve the estimates of the planet and orbital characteristics of the known planet and the methods used to investigate additional periodicity in the RV measurements.

2. Time series preparation

λ^2 For was observed by TESS in Sectors 3 and 4, for a total of approximately 2 months. The photometric time series are available in a pre-reduced version from the Science Processing Operations Center (SPOC) pipeline (Jenkins et al. 2016), as well as in the form of pixel-level data.

We attempted to manually reduce the pixel-level data using a procedure which has previously produced better signal-to-noise ratios for asteroseismic analyses of bright stars compared to the standard SPOC pipeline (Metcalfe et al. in prep). The approach broadly mirrors that used successfully on K2 data in the past (see, e.g., Buzasi et al. 2015), and revolves around defining a custom photometric aperture pixel mask. However, in the case of λ^2 For this procedure did not reduce the noise level around the p-mode envelope, but for completeness we will briefly summarize this method and the result. In the following sections we opted to only consider the SPOC time series.

2.1. Manual reduction method

For each TESS orbit we extracted a time series for each pixel and took the brightest pixel as our initial time series. The pixel time series quality figure of merit is parameterized by $q = \sum_{i=1}^{N-1} | f_{i+1} - f_i |$, where f is the flux at cadence i, and N is the length of the time series. Using the first differences of the light curve acts to whiten the time series and thus correct for its nonstationary nature (Nason 2006); similar approaches have been used in astronomical time series analysis by, *e.g.* Buzasi et al. (2015) and Prša et al. (2019).

We then iteratively added the flux of the pixels surrounding the brightest pixel. The process continued until the light curve quality stopped improving, and the resulting pixel collection was adopted as our aperture mask. The light curve produced by our aperture mask was then detrended against the centroid pixel coordinates by fitting a second-order polynomial with cross terms. Similar approaches have been used for K2 data reduction (see, e.g., Vanderburg & Johnson 2014).

Figure 1 shows the resulting time series, compared to that derived by the SPOC. In this case, low-frequency noise was somewhat improved over the SPOC light curve product, but noise levels at the frequencies near the stellar oscillation spectrum were not. We accordingly used the SPOC light curve for the analysis which follows.

3. Modeling λ^2 For

To estimate the fundamental properties of λ^2 For we used both seismic and non-seismic constraints. The seismic constraints come from measuring the individual oscillation frequencies observed in the power spectrum of the SPOC time series, also known as peakbagging. The non-seismic constraints are derived from Spectral Energy Density (SED) fitting. These constraints were then used by several independent modeling teams to provide estimates of the mass, radius and age of λ^2 For. These steps are detailed in the following section.

3.1. Seismic constraints

To measure the oscillation frequencies of λ^2 For we use the SPOC flux time series as described above. Because of the low signal-to-noise ratio of the oscillations, several independent peakbaggers[1] were tasked with finding and fitting the oscillation peaks. Initial guesses for the frequencies were found using the universal patter approach (see, Mosser et al. 2013) and by eye inspection. The final choice of frequencies was based on the subset that all teams agreed on within their respective uncertainties.

[1] Peakbagging team members: MBN, IWR, MV, BM, WJC

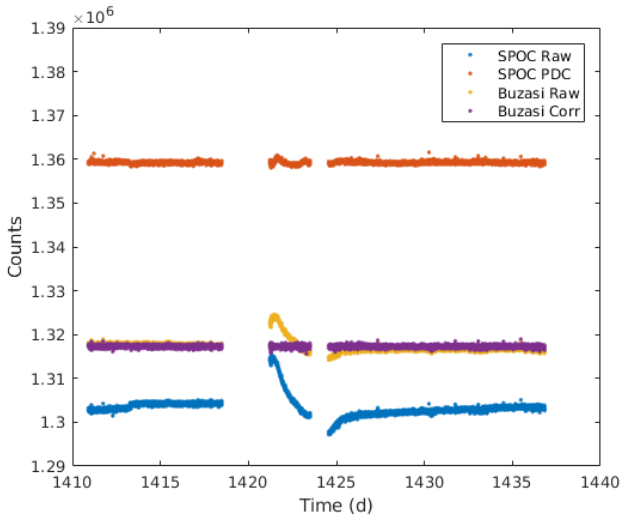

Fig. 1. Resulting counts over time for different TESS data reduction pipelines. The Buzasi Corr time series very effectively removes most of the long period variability, however the SPOC time series still shows the lowest variance in the frequency range around the p-mode envelope.

The frequencies range from 1142 μHz to 1380 μHz, with a peak of oscillation power at $\nu_{\rm max} \approx 1280\,\mu$Hz and a separation of consecutive overtones of the same angular degree (large separation), $\Delta\nu \approx 69\,\mu$Hz.

This final list of frequencies was then fit using a maximum likelihood approach with an MCMC sampler[2] (see e.g. Nielsen et al. 2017). The mode frequencies and heights were treated as independent variables for each mode, and the mode widths were assumed to follow the relation by Appourchaux et al. (2014). The fit assumed a single rotational splitting and inclination axis for all oscillation modes. The background noise level from granulation, activity and uncorrected instrumental effects were fit concurrently with the modes, using two Harvey-like profiles (Harvey et al. 1988).

The power density spectrum and the resulting fit frequencies are shown in Fig. 2, and the échelle diagram in Fig. 3. Modes of angular degree $l = 3$ were not considered by any of the teams as these are typically very low amplitude, and thus require exceptional signal-to-noise ratios to be observed. One team suggested the possible presence of mixed $l = 1$, but this could not be verified by the other teams and so these were not included in the final fit. The final list of fit frequencies is presented in Table A.1.

3.2. Non-seismic constraints

To provide non-seismic constraints for the stellar modeling, and as an independent check on the derived stellar parameters, we analysed the broadband SED together with the *Gaia* DR2 parallax, following the procedures described in Stassun & Torres (2016); Stassun et al. (2017, 2018). We gathered the $B_T V_T$ magnitudes from *Tycho-2*, the *BVgri* magnitudes from APASS, the JHK_S magnitudes from *2MASS*, the W1–W4 magnitudes from *WISE*, and the G magnitude from *Gaia*. Together, the available photometry spans the full stellar SED over the wavelength range 0.35–22 μm (see Figure 4).

We performed a fit using Kurucz stellar atmosphere models (Kurucz 2013), with the priors on effective temperature $T_{\rm eff}$, surface gravity $\log g$, and metallicity [Fe/H], from the spectroscopically determined values. The remaining free parameter is the extinction (A_V), which we restricted to the maximum line-of-sight value from the dust maps of Schlegel et al. (1998). The resulting fit (Figure 4) has a reduced χ^2 of 3.5. The best fit extinction is $A_V = 0.04 \pm 0.04$. Integrating the (unreddened) model SED gives the bolometric flux at Earth of $F_{\rm bol} = 1.36 \pm 0.05 \times 10^{-7}$ erg s cm^{-2}. Taking the $F_{\rm bol}$ and $T_{\rm eff}$ together with the *Gaia* DR2 parallax, adjusted by +0.08 mas to account for the systematic offset reported by Stassun & Torres (2018), gives the stellar radius as $R_\star = 1.64 \pm 0.08\,{\rm R}_\odot$.

3.3. Stellar modelling

Three teams, identified by their principal locations, independently fit stellar models to the seismic and non-seismic data for λ^2 For. The teams independently chose stellar evolution codes, stellar pulsation codes, non-seismic observables and fitting methods. The main choices of input physics are summarized in Table 1 and the best-fitting parameters, with uncertainties, of the models are listed in Table 2. We describe below more complicated details of the stellar models as well as how each team fit their models to the data. Our final estimates of the stellar properties are precise to 3.3 per cent in mass, 2.7 per cent in radius and 15 per cent in age.

3.3.1. Birmingham

The Birmingham team used Modules for Experiments in Stellar Astrophysics (MESA, r10398; Paxton et al. 2011, 2013, 2015) with the atmosphere models and calibrated MLT parameters from Trampedach et al. (2014a,b) as implemented in Mosumgaard et al. (2018). The mixing-length parameter in Table 1 is the calibrated correction factor that accommodates slight differences between MESA's input physics and mixing-length model and that of the simulations by Trampedach et al. (2014a,b), rather than the mixing-length parameter $\alpha_{\rm MLT}$. The free parameters in the fit are the stellar mass M, the initial metallicity $[{\rm Fe/H}]_i$ and the age t.

The objective function for the optimisation was the unweighted total χ^2 of both the seismic and non-seismic data, using observed non-seismic values of $T_{\rm eff} = 5841 \pm 60\,{\rm K}$, $\log L_\star/{\rm L}_\odot = 0.436 \pm 0.015$ and $[{\rm Fe/H}] = 0.13 \pm 0.06$, where the luminosity is derived from F_{bol} in Section 3.2, and $T_{\rm eff}$ and [Fe/H] are from Delgado Mena et al. (2017), with uncertainties increased to those used for most of the stars in Lund et al. (2017). The free parameters were optimized by first building a crude grid based on scaling relations, then optimising the best model from that grid using a combination of a downhill simplex (i.e. Nelder–Mead method, Nelder & Mead 1965) and random resampling within error ellipses around the best-fitting parameters when the simplex stagnated. Uncertainties were estimated by the same procedure as used by Ball & Gizon (2017).

3.3.2. Mumbai

The Mumbai team computed a grid of stellar models also using MESA (r10398). The grid spans masses from 1.10 to 1.38 ${\rm M}_\odot$ in steps of 0.01 ${\rm M}_\odot$, initial metallicities $[{\rm Fe/H}]_i$ from −0.02 to 0.36 in steps of 0.02 and mixing-length parameters $\alpha_{\rm MLT}$ of 1.81, 1.91 and 2.01. Gravitational settling, which is otherwise included in the stellar models, is disabled for models with $M_\star > 1.3\,{\rm M}_\odot$ but the best-fitting models are less massive and unaffected by

[2] `emcee`: Foreman-Mackey et al. (2013)

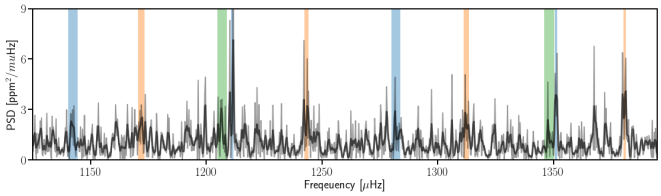

Fig. 2. Power density spectrum (grey) and the smoothed spectrum (black) around the *p*-mode oscillation frequencies. The 68% confidence interval of the fit mode frequencies are shown as the vertical shaded regions. Colors denote the angular degree, l, where blue is $l = 0$, orange is $l = 1$, and green is $l = 2$.

Table 1. Stellar model settings for the different teams. A single entry is used where all three teams used the same input physics.

Team	Birmingham	Mumbai	Porto
Models	MESA[a] (r10398)	MESA[a] (r10398)	GARSTEC[b]
Oscillations	GYRE	GYRE	ADIPLS
High-T opacities	— OPAL (Iglesias & Rogers 1993, 1996) —		
Low-T opacities	— Ferguson et al. (2005) —		
Gravitational settling	— Thoul et al. (1994) —		
EoS	MESA/OPAL	MESA/OPAL	FreeEOS
Solar mixture	GN93	GS98	GN93
Helium enrichment law ($Y = \ldots$)	$1.28855Z + 0.248$	$2Z + 0.24$	$1.1843Z + 0.2485$
Nuclear reactions	NACRE	NACRE	Solar Fusion II
Atmosphere	Mosumgaard et al. (2018)	Krishna Swamy (1966)	Eddington
$\alpha_{\rm MLT}$	1.037*	1.81, 1.91, 2.01	1.811
Surface correction	BG14-1	BG14-1	BG14-2
Overshooting	None	0 & 0.016	0.02

[a] Paxton et al. (2011, 2013, 2015) [b] Weiss & Schlattl (2008) Ball & Gizon (2014) Adelberger et al. (2011) Rogers & Nayfonov (2002) (Irwin 2012) Grevesse & Noels (1993) Townsend & Teitler (2013); Townsend et al. (2018) Herwig (2000)

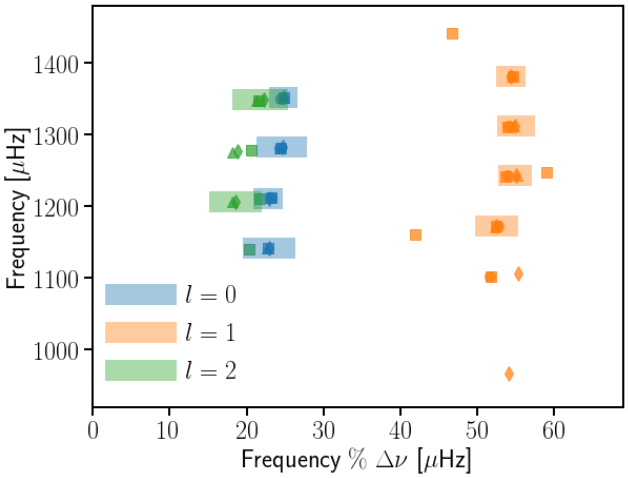

Fig. 3. Échelle diagram showing oscillation frequencies modulo the large separation ($\Delta\nu = 69.0\,\mu$Hz), supplied by each team: MV (circle), IWR (square), MBN (diamond), and WJC (triangle). The colors represent the angular degrees, l, that were considered. The shaded regions represent 68% confidence interval of the frequencies in the final fit. Several mixed modes (diverging modes along the $l = 1$ ridge) were suggested, but could not be verified by the other teams, and so were not included in the final fit.)

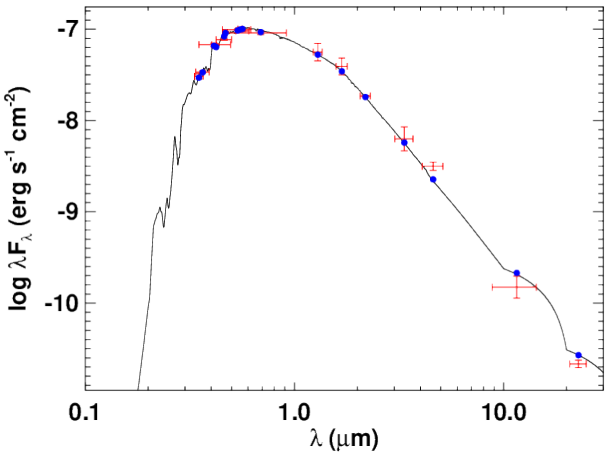

Fig. 4. Spectral energy distribution (SED). Red symbols represent the observed photometric measurements, where the horizontal bars represent the effective width of the passband. Blue symbols are the model fluxes from the best-fit Kurucz atmosphere model (black).

this choice. The grid uses two values for the length scale of core convective overshooting, using the exponentially-decaying formulation by Herwig (2000): $f_{\rm ov} = 0$ (i.e. no overshooting) and 0.016.

The goodness-of-fit was evaluated through a total misfit defined by

$$\chi^2_{\rm Mum} = (\chi^2_{T_{\rm eff}} + \chi^2_{\log g} + \chi^2_{\rm [Fe/H]} + \chi^2_{\nu})/4 \quad (1)$$

where, for $x = T_{\rm eff}$, $\log g$ or [Fe/H],

$$\chi^2_x = \left(\frac{x_{\rm model} - x_{\rm obs}}{\sigma_x}\right)^2 \quad (2)$$

and

$$\chi^2_\nu = \frac{1}{N}\sum_i \left(\frac{\nu_{i,\rm model} - \nu_{i,\rm obs}}{\sigma_{\nu,i}}\right)^2 \quad (3)$$

The observed values of the non-seismic data were $T_{\rm eff} = 5790 \pm 150$ K, $\log g = 4.11 \pm 0.06$ and [Fe/H] $= 0.09 \pm 0.11$. The reported parameters are likelihood-weighted averages and standard deviations of the likelihood evaluated for each model in the grid, where the (unnormalized) likelihood is

$$\mathcal{L}_{\rm Mum} = \exp\left(-\frac{1}{2}\chi^2_{\rm Mum}\right) \quad (4)$$

3.3.3. Porto

The Porto team used Asteroseismic Inference on a Massive Scale (AIMS: Lund & Reese 2018; Rendle et al. 2019) to optimise a grid of stellar models computed with GARSTEC (Weiss & Schlattl 2008). The observed non-seismic values were taken to be $T_{\rm eff} = 5792.5 \pm 143.5$ K, metallicity [Fe/H] $= 0.09 \pm 0.10$ and luminosity $L_\star / L_\odot = 2.71 \pm 0.10$, where the luminosity was determined from the relation by Pijpers (2003). The masses M in the grid ranged from 0.7 to 1.6 $M_\odot$ in steps of 0.01 $M_\odot$ and the initial metallicity $[{\rm Fe/H}]_i$ ranged from -0.95 to 0.6 in steps of 0.05. The models included extra mixing below the convective envelope according to the prescription by VandenBerg et al. (2012). The efficiency of microscopic diffusion is smoothly decreased to zero from 1.25 to 1.35 $M_\odot$ though, again, the best-fitting models are all significantly below 1.25 $M_\odot$ and therefore not affected by this choice. In addition, a geometric limit is applied for small convective regions, as described in Magic et al. (2010).

The goodness-of-fit function was the unweighted total χ^2 of the seismic and non-seismic data, as used by the Birmingham team (Sec. 3.3.1).

3.4. Adopted fundamental stellar parameters

Table 2 includes stellar parameter values averaged across the three stellar model fits. Specifically, we took the average and 1σ percentile ranges from the evenly-weighted combination of the three fits. For comparison, using the new scaling relation by Bellinger (2019) with $T_{\rm eff} = 5792 \pm 144$ K, [Fe/H] $= 0.09 \pm 0.10$, $\nu_{\rm max} = 1250 \pm 150$ μHz and $\Delta\nu = 69.52 \pm 1.20$ μHz, we derive a mass 1.10 ± 0.14 $M_\odot$ and radius 1.62 ± 0.07 $R_\odot$. These parameters are consistent with our adopted values $M_\star = 1.16 \pm 0.04$ $M_\odot$ and $R_\star = 1.63 \pm 0.04$ $R_\odot$, as is the radius inferred from the SED fit in Section 3.2. Figure 5 shows the $\log g$ and $T_{\rm eff}$ values estimated by each team in relation to the literature values.

4. Radial velocity analysis of the λ^2 For system

Since the discovery of λ^2 For b, a much larger sample of radial velocity data (RV) has become available from the HARPS spectrometer at the ESO La Silla 3.6m telescope. This presents an opportunity to update the orbital parameters of the planet based on this new data, and by using the new estimates of the stellar mass from asteroseismology. The HARPS data were downloaded via the ESO Science Portal[3]. We combined these data with the AAT and Keck data as presented by O'Toole et al. (2009) in Table 2 of that publication.

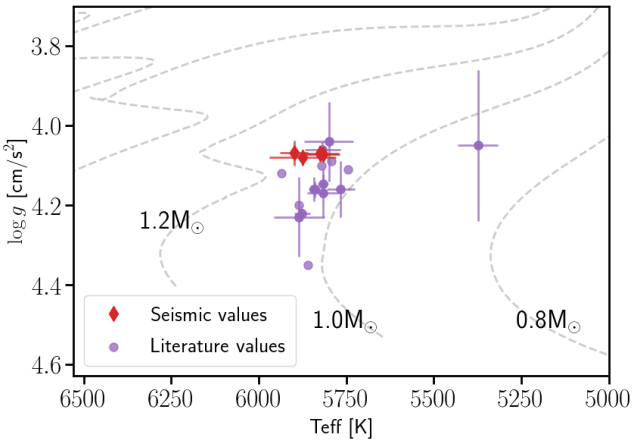

Fig. 5. Kiel diagram showing the literature values (purple) and seismic values (red, see Table 2) of λ^2 For. Dashed lines indicate evolutionary tracks spanning a mass range of $0.8 - 2\,M_\odot$, in increments of $0.2\,M_\odot$. Literature values are sources are presented in Table C.1.

4.1. Updated characteristics λ^2 For b

We used `Kima` (Faria et al. 2018) to analyze the combined dataset. `Kima` fits a sum of Keplerian curves to RV data corresponding to one or more potential planets. It uses a diffusive nested sampling algorithm (Brewer et al. 2009) to sample the posterior distribution of parameters explaining the data, where the number of planets, N_p, is left as a free parameter. This allows us to use `Kima` to estimate the fully marginalized Bayesian evidence of the parameter space, which is used to determine the likelihood of any number of planets that may be present and detectable in the data.

For the analysis of the RV data from λ^2 For, N_p was set as a free parameter, with an upper limit of $N_p = 5$. Once samples of the fit posterior were obtained from `Kima` any proposed crossing orbits were removed a posteriori. The resulting posterior consists of a wide parameter space with a number of overdensities corresponding to regions of high-likelihood for each of the parameters, such as orbital period P, semi-amplitude K, and eccentricity e. We identified such regions with the clustering algorithm `HDBSCAN` (McInnes et al. 2017). `HDBSCAN` identified a cluster corresponding to the orbital period of λ^2 For b. We extracted these samples from the posterior and used those to approximate the posterior probability density of the planetary orbital and physical parameters. As a result, we provide the median of each of parameters' distribution, and provide uncer-

[3] The HARPS dataset was collected thanks to several observing programs listed in appendix B.1, and were obtained from: https://archive.eso.org/scienceportal/home?data_release_date=*:2019-09-18&pos=39.2442,-34.57798&r=0.016667&poly=39.318719,-34.614387,39.169781,-34.614387,39.169846,-34.541445,39.318654,-34.541445&dp_type=SPECTRUM&sort=dist,-fov,-obs_date&s=P%2fDSS2%2fcolor&f=0.122541&fc=39.318654,-34.541445&cs=J2000&av=true&ac=false&c=8,9,10,11,12,13,14,15,16,17,18&ta=RES&dts=true&sdtm=%7b%22SPECTRUM%22%3atrue%7d&at=39.2442,-34.57798

Table 2. Model parameters for λ^2 For using seismic and non-seismic constraints.

Team	Birmingham	Mumbai	Porto	Adopted
Mass [$M_\odot$]	1.16 ± 0.02	1.17 ± 0.05	1.15 ± 0.03	1.16 ± 0.04
Radius [$R_\odot$]	1.64 ± 0.01	1.64 ± 0.04	1.63 ± 0.06	1.63 ± 0.04
Age [Gyr]	6.4 ± 0.5	5.6 ± 1.0	6.7 ± 0.8	6.2 ± 0.9
$T_{\rm eff}$ [K]	5816 ± 47	5861 ± 94	5824 ± 102	5834 ± 87
$\log g$ [cm/s^2]	4.07 ± 0.01	4.08 ± 0.02	4.07 ± 0.04	4.08 ± 0.03
[Fe/H]	0.12 ± 0.07	0.07 ± 0.07	0.11 ± 0.10	0.10 ± 0.08

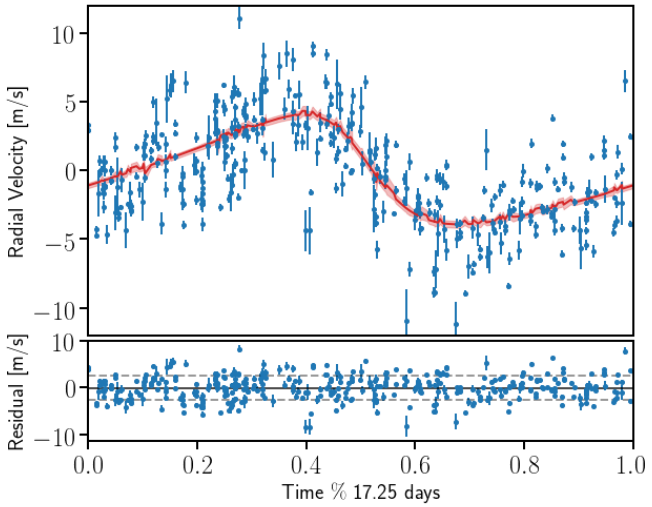

Fig. 6. Top: Observational RV data (blue) of λ^2 For, from AAT, Keck, and HARPS, phase-folded at a period of 17.25 days. The phase-folded best-fit model is shown in red, with the model uncertainties in shaded red. Bottom: Residual RV after subtracting the best-fit RV model. The dashed lines indicate the standard deviation, σ = 2.64 m/s, of the residual.

tainties estimated from the 16th and 84th percentiles which are shown in Table 3. The best-fit model is shown in Fig. 6, along with the residual RV signal which has a standard deviation of of σ = 2.64 m/s.

To verify the `Kima` results, we also fit the RV data using the `exoplanet` package (Foreman-Mackey et al. 2019), which, like `Kima`, also fits Keplerian orbits but also includes the signal from stellar granulation noise as a Gaussian process in the RV model. The `exoplanet` package uses the `celerite` library (Foreman-Mackey et al. 2017) to model any variability in the RV signal that can be represented as a stationary Gaussian process. The choice of kernel for the Gaussian process is set by the quality factor which we here chose to be $Q = 1/2$ to represent a stochastically excited damped harmonic oscillator with a characteristic timescale w_0 and amplitude S_0. We applied a normal prior on w_0 based on the modeling of the TESS power spectrum presented in Section 3, as the granulation timescale is expected to be identical in both radial velocity and photometric variability. The granulation power in the TESS intensity spectrum is not easily converted to a radial velocity signal as seen from multiple different instruments, we therefore use a weakly-informative log-normal prior on S_0. We found that the `Kima` and `exoplanet` results were consistent within 1σ.

Table 3. Best-fit orbital parameters of λ^2 For b

Parameter	Discovery paper	This work
P [days]	17.24 ± 0.01	$17.251^{+0.002}_{-0.003}$
K [m/s]	5.0 ± 0.4	4.0 ± 0.3
e	0.20 ± 0.09	$0.35^{+0.05}_{-0.05}$
$m_p \sin i$ [$M_\oplus$]	22.1 ± 2.0	$16.8^{+1.2}_{-1.3}$

Notes. Orbital parameters of λ^2 For b, where P is the orbital period, K is the RV semi-amplitude, e is the orbital eccentricity, and $M \sin i$ is the estimated lower limit of the planet mass. The middle column shows the values found by O'Toole et al. (2009), the right column shows the best-fit parameters from `Kima` found in this work.

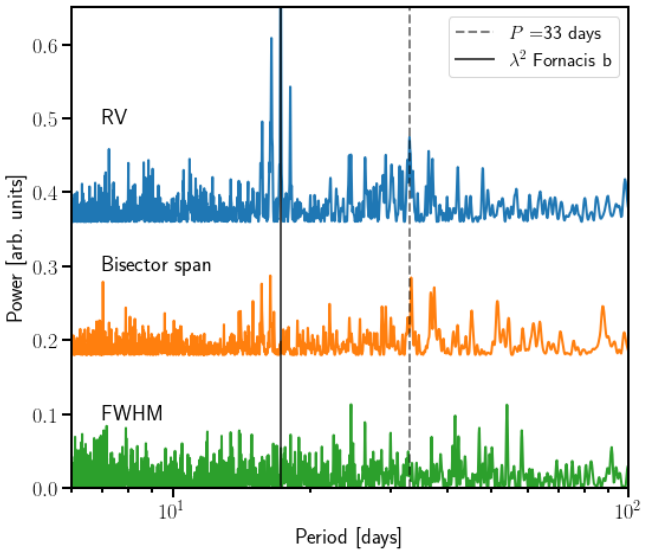

Fig. 7. Periodograms of the HARPS RV data (blue), the spectral line bisector span (orange), and the cross-correlation function full-width at half maximum (FWHM, green). The FWHM and bisector span were only available for the HARPS data, and so the AAT and Keck data are not included the power spectra shown here. The full vertical line shows the period of λ^2 For b, and the dashed line is the secondary 33 day periodicity. The comb of peaks around the orbital period of λ^2 For b are caused by the observational window function, as is the case for many of the peaks around the 33 day periodicity.

4.2. Additional radial velocity variability

O'Toole et al. (2009) suggested the presence of a periodicity at $\approx$ 298 days which they ultimately did not attribute to the presence of additional planet. The posterior distribution of the fit parameters obtained from `Kima` does indeed show a periodic-

ity at ≈ 300 days, but the Bayesian evidence does not support the added model complexity that comes from adding a planet at or near this orbital period. This was quantified by calculating the Bayes Factor (the ratio of evidence weighted probabilities, Kass & Raftery 1995) for an increase in the number of planets from $N_p = 1$, i.e. assuming only λ^2 For b exists, to $N_p = 2$. This yields a Bayes Factor of ≈ 1.67, which is "not worth more than a bare mention" (Kass & Raftery 1995). This was found to be the case when testing both just the AAT and Keck data set, as well as with the added HARPS data.

However, using the combined data sets highlights a period at ≈ 33 days. Figure 7 shows the periodogram of the RV measurements, where the signal due to λ^2 For b is visible at $P = 17.25$ days, with surrounding aliases caused by the observational window function. The 33 day periodicity also shows aliasing in the RV, but also appears in the bisector span which in addition shows harmonic peaks at a period of ≈ 16.5 days. This signal was not discussed by O'Toole et al. (2009), and so to investigate this periodicity further we established two scenarios: first, that it is due to another planet in a wider orbit than the known planet or second, that it is due to variability induced by magnetic activity on the stellar surface.

4.2.1. Scenario 1: An additional planet

The first possibility is that the 33-day signal is due to an additional planet in the λ^2 For system. Again, we used `Kima` to evaluate the possibility of a planet in such an orbit but the Bayesian evidence for the additional planet remains small. This in itself would suggest that the existence of a second planet is unlikely but as a additional measure we test the dynamical stability of such a planet to investigate if it could survive for timescales comparable to the ≈ 6.2 Gyr lifetime of the λ^2 For system.

The dynamical simulations were performed using the `REBOUND` package[4], described in detail by Rein & Liu (2012), and using the WHFast integrator (Rein & Tamayo 2015). The viability of dynamical simulations is often tested through the use of chaos indicators that quantify the divergence of planetary orbits in the system (Cincotta & Simó 1999, 2000). Such techniques have been applied to a range of exoplanetary systems (Goździewski et al. 2001; Goździewski 2002; Satyal et al. 2013, 2014; Triaud et al. 2017; Kane 2019) and provide a robust means to assess both short-term and long-term chaotic behavior within a system. The `REBOUND` code calculates a chaos indicator referred to as the Mean Exponential Growth factor of Nearby Orbits (MEGNO, Maffione et al. 2011). The MEGNO values are computed for a test particle placed in relation to the known, fixed orbit of λ^2 For b. Shown in Figure 8 are the results of our dynamical simulation, where the MEGNO values are presented as a function of eccentricity and orbital period.

MEGNO values $\lesssim 2$ indicate very likely stable orbits, while values $\gtrsim 2$ are either approaching instability (chaos), or for MEGNO $\gg 2$ have already diverged at the end of the simulation. The simulations were run for 10^5 orbits of λ^2 For b, equivalent to ≈4700 years. Figure 8 also shows the marginalized posterior distribution of the eccentricity and period obtained from `Kima`, for the 33 day periodicity. The range of periods is narrower than the symbol size (see Table 3), but the eccentricity spans a wide range. However, none of the orbits within the period range has MEGNO values $\lesssim 2$, indicating that any potential planet at this period would be quickly ejected from the system. A number of very narrow stable regions appear at multiple different periods.

[4] rebound.readthedosc.io

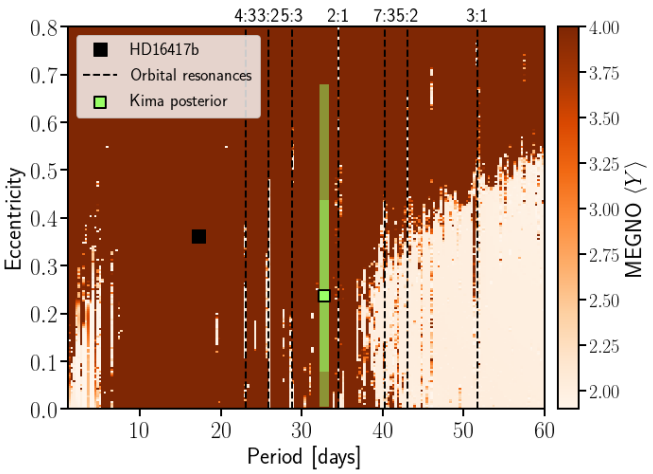

Fig. 8. Stability (MEGNO) map for a particle at different periods and inclinations, in the presence of the known planet λ^2 For b. The color bar indicates the linear scale of the MEGNO statistic, for which darker colors represent a higher degree of orbital divergence (chaos) on timescales of 10^5 orbits of λ^2 For b. Lighter shaded regions denote stable orbits. The marginalized posterior distribution of the 33 day orbit is shown in green, with the median indicated by the square symbol. Orbits in resonance with λ^2 For b are indicated by vertical dashed lines. Additional resonances are not marked for clarity. The solid black square denotes the period and eccentricity of λ^2 For b.

These are all likely due to resonances with λ^2 For b, which are indicated by the horizontal lines in Fig. 8. However, none fall near the 33 day periodicity, excluding the possibility that a planet in this orbit could be stable due to a resonance.

4.2.2. Scenario 2: Activity

While O'Toole et al. (2009) did not discus the 33 day RV variability, they estimated a rotation period of the star of 22 − 33 days, based on the measured $\log R'_{\rm HK} = -5.08$ and the age-activity relation by Wright et al. (2004). Estimates of the projected rotational velocity $v \sin i$ in the literature fall in the range 2.1 − 2.5 km/s (Nordström et al. 2004; Valenti & Fischer 2005; Ammler-von Eiff & Reiners 2012), which is consistent with a rotation period of 33 days when assuming a stellar radius of 1.633 $R_\odot$ and an inclined rotation axis on the order of $i \approx 50°$ relative to the line of sight to the observer.

While the asteroseismic fit included the rotation rate and inclination of the rotation axis of the star as free variables, the marginalized posteriors for these parameters were equivalent to the uniform priors used in the fit. The seismic fit could therefore not constrain these parameters. This is likely in part due to the low frequency resolution of the power spectrum (0.2 μHz) compared to the expected slow rotation rate of the star (≈ 0.36 μHz). Measuring rotation rates from the oscillation modes may also be further hampered by a very low angle of inclination of the rotation axis relative to the observer.

No signatures of star spots are visible in the TESS photometry, either in the SPOC or manually reduced light curves (see Fig. 1), which might also be expected for a star with a low inclination angle and low activity level.

If this signal is indeed due to rotation, a similar period is expected in the spectral line bisector and the full-width at half maximum (FWHM) of the cross-correlation function used to measure the RV (e.g. Queloz et al. 2001; Gomes da Silva et al. 2012). However, while the power spectra of the HARPS RV data

and the bisector span (see Fig. 7) show a power excess at around 33 days, the FWHM spectrum does not show any clear peaks around 33 days.

Using the gyrochronology relation by Barnes (2003), with the asteroseismic ages from Section 3 and a $B-V = 0.66$ (Ducati 2002) as input, we find that the rotation period of the star is likely between $P_{\rm rot} = 27 - 31$ days. While correcting the $B - V$ estimate for interstellar reddening decreases this estimated period range, we note that the Barnes (2003) relation is only calibrated for young main-sequence stars and does not account for structural evolution that occurs after leaving the main-sequence. This should be expected to increase the surface rotation period, as the radius of the stellar envelope increases after the main-sequence (see, e.g., Fig. 3 in van Saders et al. 2016).

5. Discussion & Conclusions

We used the recent release of TESS photometric data to perform an asteroseismic analysis of the star λ^2 For. This allowed us to place tighter constraints on the stellar parameters than has previously been possible. We measured individual oscillation mode frequencies of the star centered at $\approx$ 1280 μHz, which were then distributed to several modeling teams. Using different approaches and input physics each team returned estimates of the physical properties of the star that were consistent to within $1 - 2\sigma$. For the mass and radius, which are typically well constrained by asteroseismology, we adopted the overall values $M_\star = 1.16 \pm 0.04$ M$_\odot$ and $R_\star = 1.63 \pm 0.04$ R$_\odot$. Together with a surface temperature of $T_{\rm eff} = 5834 \pm 87$ K, this places λ^2 For firmly in the sub-giant regime.

The age of the system was less well constrained, despite the seismic constraint, with an estimate of 6.2 ± 0.9 Gyr, which is likely due to the correlation with the other model parameters. In particularly the mass and metallicity are important for estimating the age. In our case the uncertainty on the mass estimate is caused in part by the uncertainty on the mode frequencies due to the relativity short TESS time series, while the metallicity is taken from spectroscopic values in the literature.

Following this we revisited the analysis of λ^2 For b originally performed by O'Toole et al. (2009), who discovered the Neptune-like planet. We combined the radial velocity measurements from the original publication with now public HARPS measurements, yielding an RV time series spanning approximately 20 years. Using this and the seismic mass estimate, the lower mass limit of λ^2 For b was reduced from $m_p \sin i = 22.1 \pm 2.0$ M$_\oplus$ to $m_p \sin i = 16.8^{+1.2}_{-1.3}$ M$_\oplus$. The orbital eccentricity was also found to be significantly higher at $e = 0.35 \pm 0.05$, as opposed to the previous estimate of $e = 0.20 \pm 0.09$. We estimate the circularisation timescale due to tidal interaction following an expression derived in Barker & Ogilvie (2009) and find it to be $\approx$ 1120 Gyr, which is much longer than the age of the system. The slightly higher eccentricity found here is then perhaps more consistent with this long circularisation timescale, compared to the original estimate, which at a 2σ level encompasses almost circular orbits.

In addition to the revised parameters for λ^2 For b, the larger set of RV measurements also revealed a periodicity at 33 days. Despite the relatively low activity level of the star, this periodicity is more likely due to stellar rotation when compared to the case of an additional unknown planet being present in the system. Although difficult to confirm, the former scenario is consistent with the expected rotation rate of an old, inactive star like λ^2 For, and we showed that the latter scenario is not possible as such an orbit would be unstable after $\sim 10^3$ years. Assuming then that the 33 day RV signal is indeed due to rotation the relatively shorter 17.25 day orbit of λ^2 For b, means that tidal interaction with the host star will cause the planet to gradually spiral inward into the star. Using the relation by Barker & Ogilvie (2009) we can estimate the current in-fall timescale to be on the order of $10^3 - 10^4$ Gyr. This is obviously much longer than the evolutionary timescale of the host star, and so the time when the star expands to the current periastron of λ^2 For b (0.1 AU, 21.5 R$_\odot$) sets an upper limit for when the planet will be engulfed. The models presented in Section 3.3 suggest that this will happen in approximately 1.5 Gyr. However, the tidal interaction, and thus the in-fall timescale, is a strong function of the stellar radius and the orbital period (Barker & Ogilvie 2009). This will cause the in-fall to accelerate considerably over time and the planet will likely be engulfed well before λ^2 For expands to the current orbit.

Despite the rather modest time series that was obtained from TESS for λ^2 For, we have shown that it is still possible to measure individual oscillation frequencies in stars like this. This shows that asteroseismology is an important tool for obtaining tight constraints on stellar parameters, which can be applied to the enormous selection of stars being observed by TESS. This in turn prompts the re-analysis of the wealth of archival radial velocity data that has been accumulated in the last few decades for planet host stars, as the revised stellar parameters will directly impact the estimates of the planet properties.

Acknowledgements. The authors would like to thank J. P. Faria and H. Rein for useful discussions. This paper includes data collected by the TESS mission. MBN, WHB, MRS, AHMJT, and WJC acknowledge support from the UK Space Agency. AHMJT and MRS have benefited from funding from the European Research Council (ERC) under the European Union's Horizon 2020 research and innovation programme (grant agreement n° 803193/BEBOP). Funding for the Stellar Astrophysics Centre is funded by the Danish National Research Foundation (Grant agreement no.: DNRF106). ZÇO, MY, and SÖ acknowledge the Scientific and Technological Research Council of Turkey (TÜBİTAK:118F352). AS acknowledges support from grants ESP2017-82674-R (MICINN) and 2017-SGR-1131 (Generalitat Catalunya). TLC acknowledges support from the European Union's Horizon 2020 research and innovation programme under the Marie Skłodowska-Curie grant agreement No. 792848 (PULSATION). This work was supported by FCT/MCTES through national funds (UID/FIS/04434/2019). MD is supported by FCT/MCTES through national funds (PIDDAC) by this grant UID/FIS/04434/2019. MD and MV are supported by FEDER - Fundo Europeu de Desenvolvimento Regional through COMPETE2020 - Programa Operacional Competitividade e Internacionalização by these grants: UID/FIS/04434/2019; PTDC/FIS-AST/30389/2017 & POCI-01-0145-FEDER-030389 & POCI-01-0145-FEDER03038. MD is supported in the form of a work contract funded by national funds through Fundação para a Ciência e Tecnologia (FCT). SM acknowledges support by the Spanish Ministry with the Ramon y Cajal fellowship number RYC-2015-17697. BM and RAG acknowledge the support of the CNES/PLATO grant. Funding for the TESS mission is provided by the NASA Explorer Program. Based in part on data acquired at the Anglo-Australian Telescope. We acknowledge the traditional owners of the land on which the AAT stands, the Gamilaraay people, and pay our respects to elders past and present. The data presented herein were in part obtained at the W. M. Keck Observatory, which is operated as a scientific partnership among the California Institute of Technology, the University of California and the National Aeronautics and Space Administration. The Observatory was made possible by the generous financial support of the W. M. Keck Foundation. The authors wish to recognize and acknowledge the very significant cultural role and reverence that the summit of Maunakea has always had within the indigenous Hawaiian community.

References

Adelberger, E. G., García, A., Robertson, R. G. H., et al. 2011, Reviews of Modern Physics, 83, 195
Ammler-von Eiff, M. & Reiners, A. 2012, A&A, 542, A116
Angelou, G. C., Bellinger, E. P., Hekker, S., & Basu, S. 2017, ApJ, 839, 116
Appourchaux, T., Antia, H. M., Benomar, O., et al. 2014, A&A, 566, A20
Ball, W. H. & Gizon, L. 2014, A&A, 568, A123
Ball, W. H. & Gizon, L. 2017, A&A, 600, A128

Barker, A. J. & Ogilvie, G. I. 2009, MNRAS, 395, 2268
Barnes, S. A. 2003, ApJ, 586, 464
Battistini, C. & Bensby, T. 2015, A&A, 577, A9
Bellinger, E. P. 2019, MNRAS, 486, 4612
Bellinger, E. P., Hekker, S., Angelou, G. C., Stokholm, A., & Basu, S. 2019, A&A, 622, A130
Bensby, T., Feltzing, S., & Lundström, I. 2003, A&A, 410, 527
Bensby, T., Feltzing, S., & Oey, M. S. 2014, A&A, 562, A71
Bertran de Lis, S., Delgado Mena, E., Adibekyan, V. Z., Santos, N. C., & Sousa, S. G. 2015, A&A, 576, A89
Bond, J. C., Tinney, C. G., Butler, R. P., et al. 2006, MNRAS, 370, 163
Bonfanti, A., Ortolani, S., & Nascimbeni, V. 2016, A&A, 585, A5
Borucki, W. J., Koch, D., Basri, G., et al. 2010, Science, 327, 977
Brewer, B. J., Pártay, L. B., & Csányi, G. 2009, arXiv e-prints, arXiv:0912.2380
Brown, T. M., Christensen-Dalsgaard, J., Weibel-Mihalas, B., & Gilliland, R. L. 1994, ApJ, 427, 1013
Buzasi, D. L., Carboneau, L., Hessler, C., Lezcano, A., & Preston, H. 2015, in IAU General Assembly, Vol. 29, 2256843
Campante, T. L., Corsaro, E., Lund, M. N., et al. 2019, ApJ, 885, 31
Carretta, E. 2013, A&A, 557, A128
Cincotta, P. & Simó, C. 1999, Celestial Mechanics and Dynamical Astronomy, 73, 195
Cincotta, P. M. & Simó, C. 2000, A&AS, 147, 205
da Silva, L., Girardi, L., Pasquini, L., et al. 2006, A&A, 458, 609
Datson, J., Flynn, C., & Portinari, L. 2015, A&A, 574, A124
Delgado Mena, E., Tsantaki, M., Adibekyan, V. Z., et al. 2017, A&A, 606, A94
Ducati, J. R. 2002, VizieR Online Data Catalog
Faria, J. P., Santos, N. C., Figueira, P., & Brewer, B. J. 2018, Journal of Open Source Software, 3, 487
Ferguson, J. W., Alexander, D. R., Allard, F., et al. 2005, ApJ, 623, 585
Foreman-Mackey, D., Agol, E., Ambikasaran, S., & Angus, R. 2017, AJ, 154, 220
Foreman-Mackey, D., Czekala, I., Luger, R., et al. 2019, dfm/exoplanet v0.2.3
Foreman-Mackey, D., Hogg, D. W., Lang, D., & Goodman, J. 2013, PASP, 125, 306
Fridlund, M., Baglin, A., Lochard, J., & Conroy, L., eds. 2006, ESA Special Publication, Vol. 1306, The CoRoT Mission Pre-Launch Status - Stellar Seismology and Planet Finding
García, R. A. & Ballot, J. 2019, Living Reviews in Solar Physics, 16, 4
Gehren, T. 1981, A&A, 100, 97
Gomes da Silva, J., Santos, N. C., Bonfils, X., et al. 2012, A&A, 541, A9
Goździewski, K. 2002, A&A, 393, 997
Goździewski, K., Bois, E., Maciejewski, A. J., & Kiseleva-Eggleton, L. 2001, A&A, 378, 569
Gray, R. O., Corbally, C. J., Garrison, R. F., et al. 2006, AJ, 132, 161
Grevesse, N. & Noels, A. 1993, in Origin and Evolution of the Elements, ed. N. Prantzos, E. Vangioni-Flam, & M. Casse, 15–25
Harvey, J. W., Hill, F., Kennedy, J. R., Leibacher, J. W., & Livingston, W. C. 1988, Advances in Space Research, 8, 117
Hearnshaw, J. B. & Schmidt, E. G. 1972, A&A, 21, 111
Herwig, F. 2000, A&A, 360, 952
Huber, D., Chaplin, W. J., Chontos, A., et al. 2019, AJ, 157, 245
Iglesias, C. A. & Rogers, F. J. 1993, ApJ, 412, 752
Iglesias, C. A. & Rogers, F. J. 1996, ApJ, 464, 943
Irwin, A. W. 2012, FreeEOS: Equation of State for stellar interiors calculations
Jenkins, J. M., Twicken, J. D., McCauliff, S., et al. 2016, Society of Photo-Optical Instrumentation Engineers (SPIE) Conference Series, Vol. 9913, The TESS science processing operations center, 99133E
Kane, S. R. 2019, AJ, 158, 72
Kass, R. E. & Raftery, A. E. 1995, Journal of the American Statistical Association, 90, 773
Krishna Swamy, K. S. 1966, ApJ, 145, 174
Kurucz, R. L. 2013, ATLAS12: Opacity sampling model atmosphere program
Lebreton, Y. & Goupil, M. J. 2014, A&A, 569, A21
Lund, M. N. & Reese, D. R. 2018, in Asteroseismology and Exoplanets: Listening to the Stars and Searching for New Worlds, Vol. 49, 149
Lund, M. N., Silva Aguirre, V., Davies, G. R., et al. 2017, ApJ, 835, 172
Maffione, N. P., Giordano, C. M., & Cincotta, P. M. 2011, International Journal of Non Linear Mechanics, 46, 23
Magic, Z., Serenelli, A., Weiss, A., & Chaboyer, B. 2010, ApJ, 718, 1378
Mayor, M., Pepe, F., Queloz, D., et al. 2003, The Messenger, 114, 20
McInnes, L., Healy, J., & Astels, S. 2017, The Journal of Open Source Software, 2
Mosser, B., Michel, E., Belkacem, K., et al. 2013, A&A, 550, A126
Mosumgaard, J. R., Ball, W. H., Silva Aguirre, V., Weiss, A., & Christensen-Dalsgaard, J. 2018, MNRAS, 478, 5650
Nason, G. 2006, Stationary and non-stationary time series, ed. H. Mader & S. Coles (United Kingdom: Geological Society of London), 129 – 142
Nelder, J. A. & Mead, R. 1965, The Computer Journal, 7, 308

Table A.1. Oscillation frequencies ν with angular degree, l, of λ^2 For

l	ν [μHz]
0	$1142.23^{+2.08}_{-2.00}$
1	$1171.79^{+1.55}_{-1.41}$
2	$1206.95^{+1.96}_{-2.13}$
0	$1211.30^{+0.44}_{-0.69}$
1	$1243.36^{+0.80}_{-0.92}$
0	$1282.05^{+1.83}_{-1.98}$
1	$1312.27^{+1.29}_{-0.97}$
2	$1348.67^{+1.81}_{-2.70}$
0	$1351.17^{+0.43}_{-0.44}$
1	$1380.81^{+0.45}_{-0.58}$

Notes. The frequency resolution of the data set is $\Delta T^{-1} = 0.2067\,\mu$Hz

Nielsen, M. B., Schunker, H., Gizon, L., Schou, J., & Ball, W. H. 2017, A&A, 603, A6
Nordström, B., Mayor, M., Andersen, J., et al. 2004, A&A, 418, 989
O'Toole, S., Tinney, C. G., Butler, R. P., et al. 2009, ApJ, 697, 1263
Paxton, B., Bildsten, L., Dotter, A., et al. 2011, ApJS, 192, 3
Paxton, B., Cantiello, M., Arras, P., et al. 2013, ApJS, 208, 4
Paxton, B., Marchant, P., Schwab, J., et al. 2015, ApJS, 220, 15
Pijpers, F. P. 2003, A&A, 400, 241
Prša, A., Zhang, M., & Wells, M. 2019, PASP, 131, 068001
Queloz, D., Henry, G. W., Sivan, J. P., et al. 2001, A&A, 379, 279
Ramírez, I., Meléndez, J., & Asplund, M. 2014, A&A, 561, A7
Rein, H. & Liu, S. F. 2012, A&A, 537, A128
Rein, H. & Tamayo, D. 2015, MNRAS, 452, 376
Rendle, B. M., Buldgen, G., Miglio, A., et al. 2019, MNRAS, 484, 771
Ricker, G. R., Winn, J. N., Vanderspek, R., et al. 2014, in Proc. SPIE, Vol. 9143, Space Telescopes and Instrumentation 2014: Optical, Infrared, and Millimeter Wave, 914320
Rogers, F. J. & Nayfonov, A. 2002, ApJ, 576, 1064
Satyal, S., Hinse, T. C., Quarles, B., & Noyola, J. P. 2014, MNRAS, 443, 1310
Satyal, S., Quarles, B., & Hinse, T. C. 2013, MNRAS, 433, 2215
Schlegel, D. J., Finkbeiner, D. P., & Davis, M. 1998, ApJ, 500, 525
Schofield, M., Chaplin, W. J., Huber, D., et al. 2019, ApJS, 241, 12
Sousa, S. G., Santos, N. C., Israelian, G., Mayor, M., & Monteiro, M. J. P. F. G. 2006, A&A, 458, 873
Sousa, S. G., Santos, N. C., Mayor, M., et al. 2008, A&A, 487, 373
Stassun, K. G., Collins, K. A., & Gaudi, B. S. 2017, AJ, 153, 136
Stassun, K. G., Corsaro, E., Pepper, J. A., & Gaudi, B. S. 2018, AJ, 155, 22
Stassun, K. G. & Torres, G. 2016, AJ, 152, 180
Stassun, K. G. & Torres, G. 2018, ApJ, 862, 61
Thoul, A. A., Bahcall, J. N., & Loeb, A. 1994, ApJ, 421, 828
Townsend, R. H. D., Goldstein, J., & Zweibel, E. G. 2018, MNRAS, 475, 879
Townsend, R. H. D. & Teitler, S. A. 2013, MNRAS, 435, 3406
Trampedach, R., Stein, R. F., Christensen-Dalsgaard, J., Nordlund, Å., & Asplund, M. 2014a, MNRAS, 442, 805
Trampedach, R., Stein, R. F., Christensen-Dalsgaard, J., Nordlund, Å., & Asplund, M. 2014b, MNRAS, 445, 4366
Triaud, A. H. M. J., Neveu-VanMalle, M., Lendl, M., et al. 2017, MNRAS, 467, 1714
Tsantaki, M., Sousa, S. G., Adibekyan, V. Z., et al. 2013, A&A, 555, A150
Valenti, J. A. & Fischer, D. A. 2005, ApJS, 159, 141
van Saders, J. L., Ceillier, T., Metcalfe, T. S., et al. 2016, Nature, 529, 181
VandenBerg, D. A., Bergbusch, P. A., Dotter, A., et al. 2012, ApJ, 755, 15
Vanderburg, A. & Johnson, J. A. 2014, PASP, 126, 948
Weiss, A. & Schlattl, H. 2008, Ap&SS, 316, 99
Wright, J. T., Marcy, G. W., Butler, R. P., & Vogt, S. S. 2004, ApJS, 152, 261

Appendix A: Peakbagging frequencies

Appendix B: HARPS observing programs

Appendix C: Stellar properties literature sources

Table B.1. HARPS observing program PIs and IDs for data used in this work.

PI	Program ID
Diaz	198.C-0836
Doellinger	078.C-0751
Doellinger	079.C-0657
Doellinger	081.C-0802
Doellinger	082.C-0427
Hatzes	074.C-0102
Mayor	072.C-0488
Udry	091.C-0936
Udry	183.C-0972
Udry	192.C-0852

Table C.1. Literature sources for $T_{\rm eff}$ and $\log g$ values shown in Fig. 5.

Source	$T_{\rm eff}$ [K]	$\log g$
Hearnshaw & Schmidt (1972)	5793	4.09
Gehren (1981)	5860	4.35
Bensby et al. (2003)	5800 ± 70	4.04 ± 0.1
Valenti & Fischer (2005)	5817 ± 44	4.17 ± 0.06
da Silva et al. (2006)	5936 ± 70	4.12
Gray et al. (2006)	5745	4.11
Bond et al. (2006)	5374 ± 57	4.05 ± 0.19
Sousa et al. (2006)	5876 ± 22	4.22 ± 0.01
Sousa et al. (2008)	5841 ± 17	4.16 ± 0.02
Tsantaki et al. (2013)	5843 ± 12	4.16 ± 0.03
Carretta (2013)	5821	4.1
Ramírez et al. (2014)	5817 ± 15	4.146 ± 0.024
Bensby et al. (2014)	5885 ± 72	4.23 ± 0.1
Datson et al. (2015)	5766 ± 40	4.16 ± 0.07
Bertran de Lis et al. (2015)	5841	4.16
Battistini & Bensby (2015)	5885	4.2
Bonfanti et al. (2016)	5818	4.06 ± 0.02
Delgado Mena et al. (2017)	5841 ± 17	4.16 ± 0.02